Numerical simulations of gas mixing effect in electron cyclotron resonance ion sources

V. Mironov,* S. Bogomolov, A. Bondarchenko, A. Efremov, and V. Loginov
Joint Institute for Nuclear Research, Flerov Laboratory of Nuclear Reactions, Dubna, Moscow Region 141980, Russia
(Received 1 August 2016; published 26 January 2017)

The particle-in-cell Monte Carlo collisions code NAM-ECRIS is used to simulate the electron cyclotron resonance ion source (ECRIS) plasma sustained in a mixture of Kr with O_2, N_2, Ar, Ne, and He. The model assumes that ions are electrostatically confined in the ECR zone by a dip in the plasma potential. A gain in the extracted krypton ion currents is seen for the highest charge states; the gain is maximized when oxygen is used as a mixing gas. The special feature of oxygen is that most of the singly charged oxygen ions are produced after the dissociative ionization of oxygen molecules with a large kinetic energy release of around 5 eV per ion. The increased loss rate of energetic lowly charged ions of the mixing element requires a building up of the retarding potential barrier close to the ECR surface to equilibrate electron and ion losses out of the plasma. In the mixed plasmas, the barrier value is large (∼1 V) compared to pure Kr plasma (∼0.01 V), with longer confinement times of krypton ions and with much higher ion temperatures. The temperature of the krypton ions is increased because of extra heating by the energetic oxygen ions and a longer time of ion confinement. In calculations, a drop of the highly charged ion currents of lighter elements is observed when adding small fluxes of krypton into the source. This drop is caused by the accumulation of the krypton ions inside plasma, which decreases the electron and ion confinement times.

DOI: 10.1103/PhysRevAccelBeams.20.013402

I. INTRODUCTION

Mixing two gases in an electron cyclotron resonance ion source (ECRIS) is a common technique to increase currents of the highest charge states of a heavier element. This gas mixing effect was discovered experimentally by Drentje [1] in 1983. To see the effect, the flow of lighter gas into a source chamber should be much higher than the flow of the working heavier gas. Oxygen is found to be the best mixing gas for such gases as argon, krypton, and xenon, with the heavier isotope $^{18}O_2$ giving a mild improvement [2] compared to $^{16}O_2$. The gain in currents depends on the source chamber wall conditions being not pronounced when (oxidized) aluminum is used as the chamber wall material [3,4]. The negative manifestation of the effect is a drastic drop in the extracted ion currents if even very small amounts of the heavier element are present in the ECRIS plasma [5].

There are few explanations for what is happening when two gases with different masses are mixed in an ECRIS [6]. The most frequently given answer is connected to an evaporative cooling of ions [7]. Ions in the plasma are supposed to be confined within the ECR zone by a negative dip in a globally positive plasma potential [8]. The dip value is such as to equilibrate the ion and electron losses out of the plasma. The ion losses depend on ion velocities and charge states; the energetic light and lowly charged ions are leaving the trap relatively fast, which results in a cooling of those ions that remain trapped. Then, it is conjectured that in the gas mixed plasmas the ions are colder and thus are better confined by the electrostatic barrier.

At this time, no attention is paid to changes in the potential dip value when mixing two gases in the source. Also, it follows from the model that hydrogen and helium should be the best mixing gases, which is not the case. To solve the problem, it is argued that oxygen has higher ionization rates compared to helium, thus giving a higher electron density inside the ECRIS plasma and increased rates of ion production for the heavier gas [9]. Hydrogen as a mixing gas is supposed to be special because of the formation of the negative hydrogen ions, which quench the highly charged ions in the charge-change collisions. It is unclear, however, why argon is not effective as the mixing gas for such elements as krypton or xenon, having higher ionization rates compared to oxygen.

Evaporative cooling of ions is believed to be combined with the increased electron lifetime in the plasma due to the decreased electron-ion collision frequency caused by lowering the average ion charge state in the mixed plasma.

Meyer *et al.* [10] argued that the ECRIS plasma is strongly influenced by heavy ions sputtered from the source chamber walls. Fluxes of the sputtered particles depend on the energy of the ions impinging the walls and, subsequently, on the plasma potential, which is decreasing

*vemironov@jinr.ru

with the addition of light elements into the discharge. The gas mixing effect is considered from its "negative" side as the result of the source performance degradation under an influence of heavy impurities coming from the walls; authors demonstrated that a drop in the extracted currents of nitrogen ions correlates with the appearance of copper ions coming from the walls of their copper resonator used as a source chamber. There are doubts, however, whether this works for stainless steel chambers typical for ECRIS and for such working gases as xenon or krypton.

We conclude that the exact reasons for the gas mixing effect remain unknown at the moment. This motivated us to perform numerical simulations of processes in the ECRIS plasma produced in a mix of two different gases. For the study of the ECRIS, we developed a special code called NAM-ECRIS (numerical advanced model of ECRIS). The results of the calculations show that the ion temperature is actually increased in the gas mixing mode in parallel to an increase of the potential dip value. Even with an increased ion temperature, the ratio between the confining potential and the ion temperature is higher in the gas mixing mode of operation, resulting in improved ion confinement.

II. MODEL

The code is based on the model that is described in detail elsewhere [11]. NAM-ECRIS is a particle-in-cell Monte Carlo collisions code that traces the movement of macroparticles representing ions and atoms in the ECRIS plasma. The number of macroparticles (2×10^5) remains constant during the calculations with particle statistical weight used as an input. Another input is the temperature of electrons inside the ECR volume (T_{ew}), which is varied in the range of a few keV. The electron temperature outside the ECR volume is always set to 5 eV. The electron density is calculated from a charge-neutrality requirement; it is the sum of ion charge densities inside a computational cell.

In the calculations, the plasma is characterized with two important values—the gas flow in and out of the source chamber and the power carried away to the chamber walls by the lost electrons. The values are calculated from the full ion current out of the plasma for the power and from the particle flow into an extraction aperture for the gas flow.

Charged particles undergo elastic and inelastic ion-ion and electron-ion collisions, charge-change collisions with neutral particles, and neutralizing collisions with the source chamber walls.

A. Fields and geometry

Computational particles are moving in the magnetic field of the ECRIS. The solenoidal component of the field is calculated with the POISSON/SUPERFISH code [12]. The multipole component is calculated analytically in the hard-edge approximation. We perform calculations for the geometry and the magnetic field structure of a DECRIS-SC2 18 GHz source [13]. The inner diameter of the source chamber is 7.4 cm, the chamber length between the biased disk and the extraction electrode is 28 cm, and the chamber is made of stainless steel. The diameter of the extraction aperture is 1 cm. The hexapole magnetic field at the radial wall is 1.1 T, and the magnetic fields at the axis at the injection and extraction sides of the chamber are 1.97 and 1.35 T, respectively. The minimum field is 0.47 T. The magnetic configuration is selected close to the experimentally found optimum for the medium-charged ($Q \sim 8+$) argon ion production. Calculations are performed for 18 GHz microwaves resulting in 0.643 T of the electron cyclotron resonance value of the magnetic field.

B. Potential dip and lifetimes

To see the gas mixing effect, the model should be modified compared to the version described in Ref. [11]. We assume that the ion motion is affected by the dip ($\Delta\varphi$) in the positive plasma potential. The dip or jump in the plasma potential occurs at the ECR surface. The code fixes the moment when an ion crosses the ECR surface; the component of ion velocity along the magnetic field line is calculated. There are two possibilities—the ion moves either out of the zone or into the zone. If the ion leaves the ECR volume and its kinetic energy along the line is less than $Q \times \Delta\varphi$ (Q is the ion charge state), the ion is reflected back from the barrier elastically. If the ion is energetic enough to overcome the barrier, its velocity along the magnetic field line is decremented by the corresponding value. If the ion moves into the ECR volume from outside, it is accelerated along the magnetic field line with the energy gain $Q \times \Delta\varphi$.

The potential dip $\Delta\varphi$ is selected such as to provide that the calculated ion and electron confinement times in the plasma are equal each with an allowance of $\pm 5\%$. The global ion confinement time is calculated as the ratio between the total number of ion charges inside the ECR volume and the total ion current (I_i) toward the source chamber walls and into the extraction aperture:

$$\tau_i = \frac{\sum_Q (Q \times \int_{\mathrm{ECR}} n_{iQ}(x,y,z)dV)}{I_i}. \tag{1}$$

The charge state resolved confinement times of ions are calculated in the same manner:

$$\tau_{iQ} = \frac{Q \times \int_{\mathrm{ECR}} n_{iQ}(x,y,z)dV}{I_{iQ}}. \tag{2}$$

When appropriate, we compare the calculated ion confinement times with the estimation given by Rognlien and Cutler [14] for the highly collisional ions:

$$\tau_{iQ} = \frac{\sqrt{\pi}RL}{v_i} \exp\left(\frac{Q\Delta\varphi}{T_i}\right). \tag{3}$$

Here, L is length of the system (close to the length of the ECR volume, $L = 7.3$ cm in our conditions), T_i is the ion

temperature, R is the mirror ratio ($R = B_{\max}/B_{\min}$, where $B_{\max}$ and $B_{\min}$ are the maximal and minimal magnetic fields of the magnetic trap, respectively; for this specific case $B_{\max} = 0.643$ T, and the mirror ratio is calculated along all magnetic field lines within the ECR volume, $R = 1.25$), and $v_i = \sqrt{2T_i/M_i}$ is the ion velocity (M_i is the ion mass). The authors of Ref. [14] estimate that the times (3) are accurate for moderately large mirror ratios and barrier heights ($Q/\Delta\varphi \geq 3T_i$).

The electron losses are calculated by using the following expression:

$$\nu_e = \tau_e^{-1} = g(R)(\nu_{ei} + \nu_{ee}) + \varepsilon(R, T_{ew}) \frac{P_{\rm rf}}{V\langle n_e\rangle T_{ew}} + f(R, E_{\rm sec})\nu_{\rm ion}. \quad (4)$$

The first term in the sum accounts for the electron losses into the loss cone due to electron-electron and electron-ion collisions. The corresponding average 90° scattering frequencies are [15]

$$\nu_{ee} = 2.9 \times 10^{-12} \frac{\langle n_e\rangle}{T_{ew}^{3/2}} \lambda_{ee};$$
$$\nu_{ei} = 4.1 \times 10^{-12} \frac{\sum_Q \langle n_{iQ}\rangle \times Q^2}{T_{ew}^{3/2}} \lambda_{ei}. \quad (5)$$

Here, electron $\langle n_e\rangle$ and ion densities $\langle n_{iQ}\rangle$ ([m^{-3}]) are averaged over the ECR volume; λ_{ee} and λ_{ei} are the Coulomb logarithms for electron-electron and electron-ion collisions, respectively, and T_{ew} is the electron temperature [eV] inside the ECR volume. The $g(R)$ factor in (4) depends on the magnetic trap mirror ratio R. We use the mirror ratio averaged over all magnetic field lines that cross the ECR volume, taking as $B_{\max}$ the magnetic fields at the points where lines cross the source walls; $R = 2.3$ for the DECRIS-SC2 18 GHz source.

For $g(R)$ the estimation from Post [16] is

$$g(R) = \frac{R + 1.5}{R - 1} = 2.9. \quad (6a)$$

We note here that the Pastukhov time [17], which is often used for calculations of electron losses out of the magnetic trap of an ECR plasma, is derived for $R \gg 1$ and underestimates the electron loss rate in our case by a factor of ~3 compared to the Post time:

$$g(R) = \left[\frac{\sqrt{\pi}}{4}\sqrt{1 + \frac{1}{R}}\ln\left[\frac{\sqrt{1 + 1/R} + 1}{\sqrt{1 + 1/R} - 1}\right]\right]^{-1} = 0.8. \quad (6b)$$

The second term in (4) describes the electron losses due to the pitch-angle scattering of electrons by microwaves [18]. There, $P_{\rm rf}$ is the total microwave power absorbed by electrons [eV/sec] and V is the plasma volume [m^3], which is supposed to be equal to the ECR volume. For $\varepsilon(R, T_{ew})$ we use the results of the Fokker-Planck calculations of Cluggish, Zhao, and Kim [18], fitting them with a linear dependence on the electron temperature:

$$\varepsilon(R, T_{ew}) = 0.32 \times \left(\frac{3}{2} T_{ew}/4 \times 10^4\right). \quad (7)$$

Cluggish, Zhao, and Kim argue that ε should depend on the magnetic trap profile and on the shape of the electron distribution function (EDF) in velocity space, independent of the mean electron energy, electron density, and microwave power. The fact that the factor ε is increasing with the mean electron energy in their calculations when changing the gas pressure was attributed to be caused by changes in the EDF.

The third term $f(R, E_{es})$ in (4) represents the electron losses that occur soon after the creation of secondary electrons in the ionizing collisions [18]. In our model, all newborn electrons are supposed to have an isotropic distribution in velocity space and energies E_{es} equal to the ionization potential of the ionized particle [19]. We calculate the probability for the newborn electron to be in the loss cone by saving the starting coordinates of the electrons and their energies for a large number of ionizing events; the coordinates and energies are then imported into the special code that traces the electron movement in the source magnetic field. In the code, electrons are supposed to be reflected back from the thin sheath adjacent to the walls if their energy along the magnetic field line is less than 25 eV, which corresponds to the typical value of the plasma potential. Electrons are traced for a sufficiently long time to calculate the number of electrons lost to the walls while bouncing and drifting inside the magnetic trap. Electron scattering in collisions with ions and other electrons is omitted. The procedure is repeated several times during the calculations to prove that the $f(R, E_{\rm sec})$ value is stable with an accuracy of ±5%. Typical values of the lost electron fraction are in the range 0.05–0.2; the largest values are calculated for krypton because of the relatively large energies of the newly created electrons. Without taking into account the electron retardation by the positive plasma potential, the lost electron fraction is 0.3 with no dependence on the electron starting energies.

All factors in (4) are defined with a rather large uncertainty. We use them as the first approximation, keeping in mind that separate investigations are needed to calculate the electron losses in a more accurate way. The electron losses out of the plasma are calculated without taking into account the losses caused by the plasma microinstabilities, which may seriously degrade the source performance at the highest electron temperatures.

C. Wall neutralization processes

Gas in the source chamber is heated due to incomplete energy absorption by the chamber surface after the

neutralization of energetic ions impinging the walls. We distinguish between light (lighter than atoms of the wall material) and heavy ions: the heavy ions are supposed to be completely thermalized after their reflection; for the light ions we use the energy accommodation coefficients from Ref. [20]. The energy accommodation coefficient is defined as $\alpha = (E_r - E_i)/(E_i - E_w)$. Here, E_r and E_i are energies of the reflected and incident particles, respectively, $E_w = \frac{3}{2}kT_w$ is the mean energy of the wall atoms, and T_w is the surface temperature. The energy accommodation coefficient depends on the angle of incidence of the projectile (θ) and on the ratio between the masses of projectile and wall atoms ($u = M_g/M_w$, $M_w = 56$), $\alpha = 3.6u\sin\theta/(1+u)^2$. We set the primary energy of ions equal to $25 \times Q$ eV (assuming the plasma potential of 25 V), and the angle of incidence for ions is close to the normal with respect to the surface ($\sin\theta = 1$); for the subsequent collisions of the thermalizing atoms with the walls, we use an averaged value for $\overline{\sin\theta} = \sqrt{2}/2$. All ions are supposed to be neutralized after their reflection from the surface. For helium, the reflected atoms carry away almost 80% of their primary energy, 20 or 40 eV depending on the ion charge state. Each time the thermalizing atoms hit the surface, they lose some fraction of their energy and then move slower; the time of residence in the source chamber steadily increases while atoms are cooling. The result is the presence inside the source of the suprathermal atoms with the mean energy of ~0.1 eV.

For the atomic oxygen, we take into account a high probability for the atom recombination in collisions with the walls with forming the molecular oxygen ($\alpha_r \sim 0.5$ for the stainless steel surfaces) [21]. We assume that the formed molecular oxygen is fully thermalized. The recombination probability is relatively small for the atomic nitrogen ($\alpha_r \sim 0.01$) [22], as well as for collisions of atomic oxygen with oxidized surfaces—for quartz surfaces, the coefficient can be as small as $\alpha_r \sim 10^{-4}$ [23].

D. Ionization processes

Ionization rates for the light ions ($Z \leq 30$) are taken from the fits of Ref. [24]. For krypton we use the fits from Ref. [25] for all charge states except Kr^0. For the atomic krypton we use the cross sections from Ref. [26], taking into account large errors in the ionization rates of the lowly charged ions in Ref. [25]. Scaling from Ref. [27] is used for the multiple ionization rates for all gases except argon. For argon, rates for the double ionization are taken from Ref. [28]. The ionization and dissociation dynamics of the neutral and singly charged oxygen and nitrogen molecules is treated by taking into account the reactions listed in Table I. For comparison, the ionization rates for the oxygen and nitrogen atoms are also given in Table I.

The molecular dissociative recombination rates are calculated with the fits from Refs. [31,34]. The rates are non-negligible only for the cold electrons ($T_{ec} = 5$ eV), and the recombination is taken into account for the regions outside the ECR volume. It is seen that after the dissociation of molecules the singly charged ions and atoms of oxygen and nitrogen are born with relatively high energies. The oxygen fragments are more energetic compared to nitrogen.

The accepted general procedure of the numerical simulations is as follows: we fix the desired level of the coupled microwave power and choose the electron temperature inside the ECR volume. The potential dip value is selected to ensure that the electron and ion confinement

TABLE I. Ionization rates (k, 10^{-8} cm^{-3}/ sec) and kinetic energy release (KER) per fragment [eV] for molecular oxygen and nitrogen ($T_{ew} = 12$ keV).

	Reaction	k	KER	References
1	$O_2 + e \rightarrow {O_2}^{1+} + 2e$	5.5	0	[29]
2	$O_2 + e \rightarrow O + O + e$	3.3	1	[29]
3	$O_2 + e \rightarrow O + O^{1+} + 2e$	1.8	3.5	[29]
4	${O_2}^{1+} + e \rightarrow {O_2}^{2+} + 2e \rightarrow O^{1+} + O^{1+} + 2e$	1.0	6.5	[30]
5	${O_2}^{1+} + e \rightarrow O^{1+} + O^{1+} + 2e$	1.2	6.5	[30]
6	${O_2}^{1+} + e \rightarrow O^{1+} + O + e$	1.8	3.5	[30]
7	${O_2}^{1+} + e \rightarrow O + O$	1.0 ($T_e = 5$ eV)	1	[31]
	$O + e \rightarrow O^{1+} + 2e$	1.4	0	[24]
8	$N_2 + e{N_2}^{1+} + 2e$	7.1	0	[32]
9	$N_2 + e \rightarrow N + N + e$	3.9	0.5	[32]
10	$N_2 + e \rightarrow N + N^{1+} + 2e$	0.9	3.2	[32]
11	$N_2^{1+} + e \rightarrow N_2^{2+} + 2e \rightarrow N^{1+} + N^{1+} + 2e$	1.6	5.9	[33]
12	$N_2^{1+} + e \rightarrow N^{1+} + N^{1+} + 2e$	0.6	5.9	[33]
13	$N_2^{1+} + e \rightarrow N^{1+} + N + e$	1.6	3.2	[33]
14	$N_2^{1+} + e \rightarrow N + N$	2.2 ($T_e = 5$ eV)	0.5	[34]
	$N + e \rightarrow N^{1+} + 2e$	1.3	0	[24]

times are equal to each other; the particle statistical weight is adjusted to reach the selected level of the coupled power.

III. RESULTS

A. Injection of one gas

We begin with showing the charge state distributions (CSDs) of the extracted ions without mixing the gases. The spectra for the krypton plasma are presented in Fig. 1 for two electron temperatures T_{ew} (8 and 16 keV) and for the coupled microwave power $P_{\rm rf} = 500$ W; spectra for the oxygen plasma are shown in Fig. 2 for the same electron temperatures and power. If the coupled microwave power is fixed at some level, a plasma with the lower electron temperature is obtained by increasing the gas flow. An increase in the gas flow results in a global shift of CSDs to the lower charge states with an increase in the currents of the lowly charged ions and with a decrease in the currents of the highest charge states. This global tendency is often observed in practice.

There is an anomaly in the krypton CSD at a charge state (8+). This is explained by the relatively high ionization rate for Kr^{8+} ions. Another set of ionization rates [35] also shows this anomaly. Measurements confirm a local decrease of the extracted ion currents for this charge state [36].

The currents of oxygen ions are much higher compared to krypton, with the current of O^{6+} reaching the 1 mA level. The shape of the CSDs is close to what is experimentally observed.

The calculated parameters of the krypton and oxygen plasmas in these conditions (plus the intermediate cases of $T_{ew} = 12$ and 4 keV) are listed in Table II. The parameters of the plasmas are also shown for $T_{ew} = 4$ and 12 keV for the injection of helium, neon, argon, and nitrogen gases for the same 500 W of coupled power.

In Table II, the values are given for the gas flow into the source in particle-mA (for oxygen and nitrogen, flows of the oxygen and nitrogen atoms are given, ×2 of the molecular flow), currents of the extracted ions for the representative charge states, potential dip $\Delta\varphi$, electron confinement time τ_e, ion temperatures for ions inside the ECR volume, and the mean electron density inside the ECR volume.

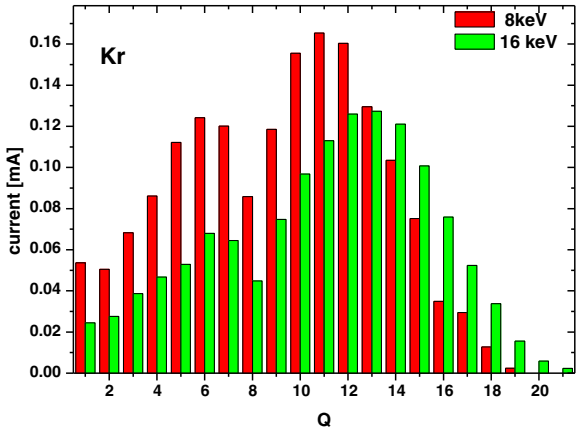

FIG. 1. Charge state distribution of the extracted krypton ions for the electron temperatures of 8 and 16 keV.

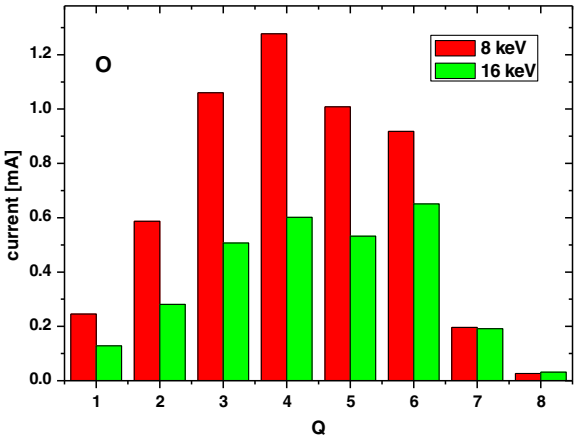

FIG. 2. Charge state distribution of the extracted oxygen ions for the electron temperatures of 8 and 16 keV.

The largest potential dip values $\Delta\varphi$ are observed for the oxygen plasma, and the lowest dips are seen for the krypton plasma. In the descending $\Delta\varphi$ order, the elements are sorted as $O_2 \rightarrow N_2 \rightarrow He \rightarrow Ne \rightarrow Ar \rightarrow Kr$. The ion temperatures follow the same tendency, being maximal for the oxygen plasma. A very large difference in the $\Delta\varphi$ values between discharges in the molecular and inert gases is caused by the strong heating of the oxygen and nitrogen singly charged ions after the dissociation of the molecules.

The electron confinement times are largest for He and lowest for Kr; the ordering of elements with the descending confinement times is $He \rightarrow N_2 \rightarrow O_2 \rightarrow Ne \rightarrow Ar \rightarrow Kr$. The electron density has the same ordering, being maximal for the lightest element in the sequence. We note that the difference in the electron confinement times is not very strong, varying by a factor of around 2 comparing krypton and helium.

Most of the electron losses from the plasma are caused by the electron-ion scattering process: for krypton, losses due to the electron-electron scattering [Eq. (4)] are equal to around 5% of the total losses, while the rf-induced scattering of electrons contributes to ≈20% of the total losses at $T_{ew} = 12$ keV. For helium, the budget of electron losses is as follows: 20% are due to the electron-electron collisions, 20% are caused by the rf-induced loss-cone scattering, and the remaining 60% of losses are the result of electron-ion collisions. In addition, 18% of all newborn electrons are lost soon after their creation for the krypton plasma [factor $f(R, E_{\rm sec})$ in Eq. (4)]. This value for the helium plasma is almost the same, $f(R, E_{\rm sec}) = 0.12$.

Experimentally, the contribution of the rf-induced losses of electrons can be estimated by measuring, e.g., the electron current to the biased disk after switching off the

TABLE II. Main parameters of the plasma with injecting one working gas (krypton, oxygen, helium, neon, argon, and nitrogen). The coupled microwave power is 500 W.

Z	T_{ew}, keV	Flow, pmA	$I_i(Q)$, μA	$\Delta\varphi$, V	τ_e, ms	T_i, eV	n_e, 10^{12} cm^{-3}
Kr	4	0.77	221(12+)	−0.017	0.14	0.24(12+)	0.8
Kr	8	0.33	160(12+)	0.002	0.29	0.27(12+)	0.82
Kr	12	0.25	146(12+)	0.008	0.41	0.31(12+)	0.81
Kr	16	0.2	126(12+)	0.012	0.55	0.32(12+)	0.77
O	4	3.0	894(6+)	0.66	0.19	3.17(6+)	1.06
O	8	1.74	918(6+)	0.94	0.37	2.91(6+)	1.19
O	12	1.2	816(6+)	1.1	0.54	2.85(6+)	1.25
O	16	0.9	650(6+)	1.18	0.73	2.76(6+)	1.25
He	4	8.45	7210(2+)	0.22	0.23	0.4(2+)	1.52
He	12	3.18	3170(2+)	0.7	0.78	0.615(2+)	1.75
Ne	4	2.84	1320(6+)	0.04	0.19	0.57(6+)	1.0
Ne	12	0.88	460(6+)	0.2	0.54	0.71(6+)	1.15
Ar	4	2.06	1450(8+)	0.015	0.17	0.7(8+)	0.93
Ar	12	0.6	500(8+)	0.075	0.5	0.56(8+)	0.97
N	4	3.48	2020(5+)	0.6	0.19	2.4(5+)	1.17
N	12	1.28	991(5+)	1.0	0.58	2.35(5+)	1.27

rf heating of the plasma [37]. The typical drop of the current is around 50%, indicating a possible underestimation of the loss rate in our model. Definitely, more study of the subject is needed.

For all investigated gases, an increase in the gas flow (decrease in the electron temperature) results in a decrease of the electron confinement time and in lower potential dip values. The electron density is slightly decreasing with increasing the gas flow; changes in the electron confinement times are mainly due to the dependence of the electron scattering frequencies on the electron temperature $\sim T_{ew}{}^{3/2}$; see Eqs. (4) and (5). The potential dip value drops fast for the krypton and relatively slow for the oxygen plasma. For krypton, the dip value is close to zero at an electron temperature around 8 keV and changes its sign with further increasing the gas flow and decreasing the electron temperature in order to maintain the balance between electron and ion losses. Neon and argon plasmas show the same tendency, but for them the potential dip approaches zero at an electron temperature of ∼3 keV for the same coupled microwave power of 500 W.

The ion temperatures for krypton and other inert gases (except argon) are decreasing with increasing the gas flow into the source, even if the ion heating rate is higher for the lower electron temperatures—a higher heating rate is overcompensated by the decreased potential dip value and by the decreased time of ion confinement in the plasma. For oxygen and nitrogen, the ion temperature is increasing with the gas flow: a decrease of the dip is not so pronounced for these plasmas, and the ion heating rate is mainly determined by the dissociation of molecules.

In contrast to oxygen, currents of the moderately charged nitrogen ions do not saturate with lowering the electron temperature, reaching 2 mA for N^{5+}. This difference is due to the relatively fast decrease of ionization rates for the production of the highly charged oxygen ions (6+ and higher) at low electron temperatures compared to nitrogen.

B. Injection of two gases

When krypton is mixed with a lighter gas, a pronounced gain in the currents of the highest charge states of krypton ions can be obtained if the flows of the light and main gases are optimized. The typical spectra of the extracted ion currents for pure krypton and for krypton mixed with oxygen are shown in Fig. 3. Here, the electron temperature is set to 12 keV, the coupled power is set to 500 W, and the number of oxygen atoms in the source chamber is 85% of the total number of macroparticles. The mix ratio and the electron temperature are selected such as to maximize the extracted Kr^{18+} ion currents. In the mix, currents of Kr ions

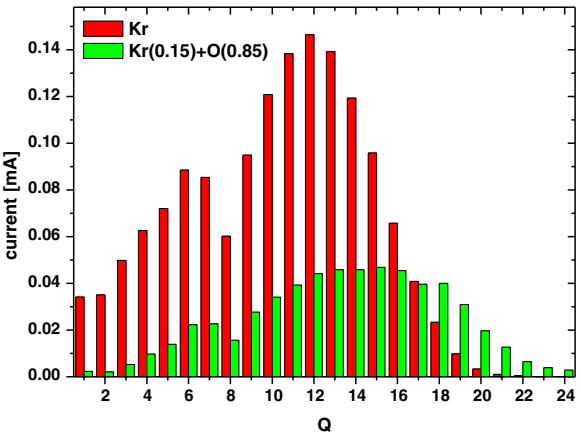

FIG. 3. Charge state distribution of the extracted krypton ions in the krypton discharge (red) and in the mix of krypton and oxygen (green).

with the charge states ≥18+ increase, and currents of lowly charged ions decrease.

In the krypton nonmixed discharge, the current of Kr^{18+} ions is maximized at a larger electron temperature, $T_{ew} = 16$ keV. When comparing the maxima of Kr^{18+} currents for the krypton and oxygen-mixed plasmas, they differ not so much (∼15%) as the currents at the same electron temperature of 12 keV. In the following sections, we will focus on the data obtained at the electron temperature that is optimal for Kr^{18+} ion production in the mix.

We present the data obtained with the fixed power of 500 W. The selection is rather arbitrary: the calculated extracted current of O^{6+} ions is at the level of around 1 mA at this power, close to what is measured with the DECRIS-SC2 source when the injected microwave power is 600 W. As is discussed in Ref. [11], the value of the coupled power as it is used in our model can substantially differ from the experimentally measured injected power both due to the incomplete microwave absorption in the plasma and due to deviations of the electron energy distribution function from the Maxwell-Boltzmann distribution.

1. Mix with oxygen

The dependence of the extracted Kr^{18+} ions on the mix ratio is shown in Fig. 4. The currents are calculated at an electron temperature of 12 keV. The oxygen content is varied from 0 to 100%. The current of the krypton ions drops by a factor of ∼2 when a small amount (5%–10%) of oxygen is added to the discharge; then it grows up and is maximized at 85% of oxygen content. For the oxygen content above the optimal value, the current of krypton ions decreases fast.

When changing the oxygen content, gas flows of krypton and oxygen vary almost linearly. For the krypton plasma (with no oxygen) the gas flow is 0.2 p-mA; for the oxygen plasma (with no krypton) the flow is 1.2 p-mA. The current of Kr^{18+} is maximized when the oxygen flux is much higher than the krypton flux; the ratio between the fluxes is ∼14 for an oxygen content of 85%.

The ion density of the krypton ions varies with changing the oxygen content slower than the krypton flow. Even for a small krypton content, the mean density of krypton ions is comparable to the density of oxygen ions inside the ECR volume: the ratio between oxygen and krypton densities is 5.3 for an oxygen content of 95%, while the ratio between the gas flows is 63 in these conditions. This is an indication of an increased krypton ion confinement at high oxygen content.

The mean charge state of the krypton ions inside the dense parts of the plasma is increasing with increasing the oxygen and krypton mixing ratio. This is illustrated by Fig. 5, where the mean charges of krypton and oxygen ions are shown for different oxygen contents. For the oxygen ions, the mean charge state does not vary significantly with changing the krypton content in the wide range down to Kr = 5% being at the level of ∼(2+), much lower compared to the pure oxygen plasma (Kr = 0%), for which it is close to (4+). For the krypton ions, the mean charge state is increasing when adding more oxygen into the plasma and reaches (14+) at Kr = 5%, almost doubling compared to the pure krypton plasma.

The mean electron density inside the ECR volume is not changing significantly for different oxygen mixings, being at the level of 8×10^{11} cm^{-3}. The only change is a fast increase in the density for the O = 100% case. There, the electron density is noticeably higher and reaches 1.25×10^{12} cm^{-3} (see also Table II).

The electron confinement time is at the level of 0.4 ms for all plasmas with nonzero krypton content. Again, there is a jump in the electron confinement time in the case of O = 100%, for which it is increased up to 0.54 ms.

For all investigated mixes, the electron confinement time is mostly determined by the electron-ion scattering; for the nonzero krypton contents, the contribution into the total scattering frequency of electron scattering on the krypton

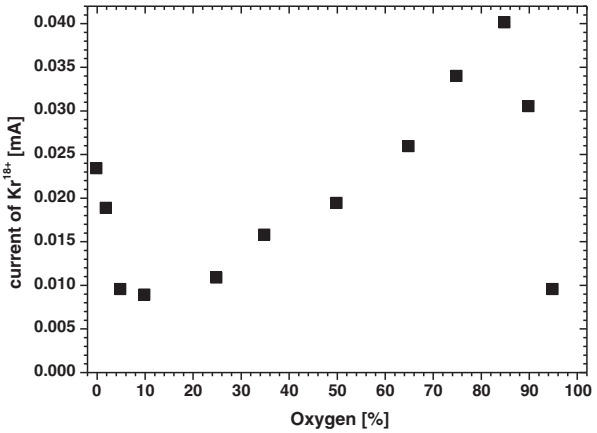

FIG. 4. Extracted current of Kr^{18+} ions for different oxygen contents.

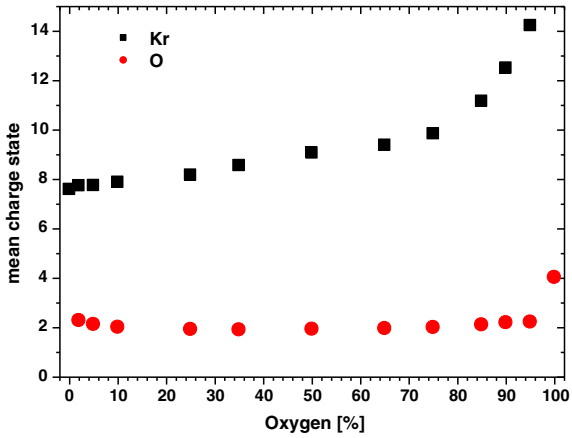

FIG. 5. Mean charge state of the krypton and oxygen ions inside the ECR volume for different oxygen contents.

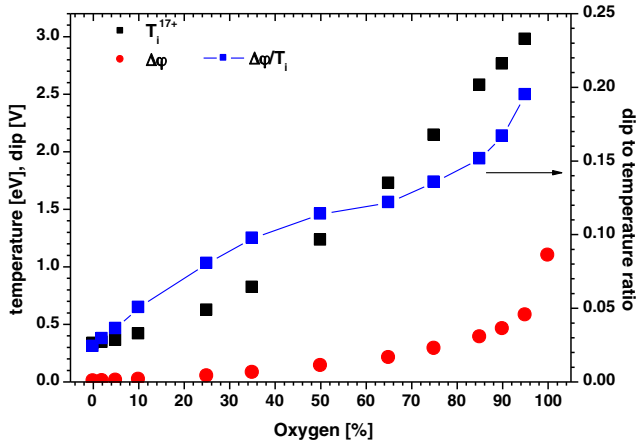

FIG. 6. Potential dip $\Delta\varphi$ (red circles, left scale), temperature of Kr^{17+} ions (black squares, left scale), and the ratio between these values (line with blue squares, right scale) for different oxygen contents.

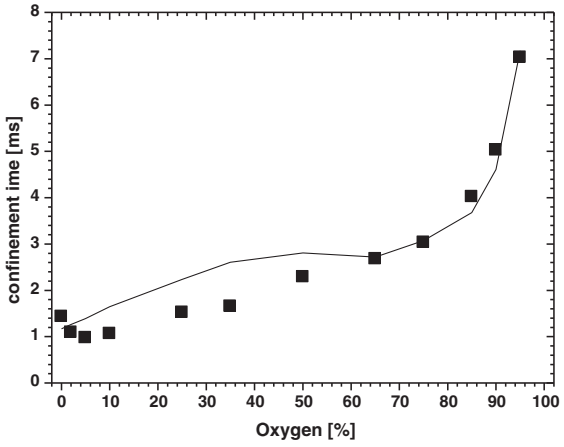

FIG. 7. Confinement time of Kr^{17+} ions for different oxygen contents. The fit with the Rognlien-Cutler times is shown as a line.

ions is determinative. Even for the limiting krypton content Kr = 5%, when the krypton flux into the source is much lower than the flux of oxygen, the frequency of electron-krypton collisions is ~95% of the total electron-ion scattering frequency. As it is following from Eq. (5), the electron-ion frequency scales as $\sim Q^2$, where Q is an ion charge state. Even with having the relatively small densities, the krypton ions scatter the plasma electrons more frequently because of their high mean charge state.

The increased oxygen content leads both to an increase of the potential dip value and to an increase of the ion temperatures. The dependencies of $\Delta\varphi$ and the temperature of Kr^{17+} ions inside the ECR volume are shown in Fig. 6, as well as a ratio between the dip and ion temperature $\Delta\varphi/T_i(Kr^{17+})$. The charge state (17+) is selected because these ions are a source for the production of Kr^{18+} ions, and we are mainly focused on the extracted currents of Kr^{18+} ions in our analysis.

With adding more oxygen into the plasma, the dip is growing faster than the ion temperature, resulting in the increasing $\Delta\varphi/T_i(Kr^{17+})$ and in the stronger ion confinement.

More details of changes in ion confinement are given in Fig. 7, where the confinement time of Kr^{17+} ions is plotted as a function of the oxygen content. The time is calculated by using Eq. (2); a fast increase in the confinement time is seen. The time is increased by a factor of almost 3 at the optimized mix of O = 85% compared to the krypton plasma. It is also seen that an injection of a small amount of oxygen results in a decrease of the ion confinement time by around 30%.

The dependence of the ion confinement time is fitted in Fig. 7 with the "Ronglien-Cutler"-type curve:

$$\tau_{iQ} = \frac{A}{9.79\times 10^3\sqrt{2T_{iQ}/M_i}}\exp(Q\Delta\varphi/T_{iQ}),$$

where A is the fitting coefficient [m], M_i is the ion mass in atomic units, and 9.79×10^3 m/sec is the unit conversion factor. The fitting coefficient of the curve in Fig. 7 is $A = 0.68$ m. The estimate from Eq. (3) gives $A = 0.16$ for $R = 1.25$ and $L = 0.073$ m; the times in Fig. 7 correspond to $\approx 4.25\tau_{(\text{Ronglien-Cutler})}$ for the high and very small oxygen contents.

Strong deviations from the fitting curve are seen for the low and intermediate oxygen contents in the range from 5% to 65%.

The drop in the extracted krypton ion current (Fig. 4) and the decrease of the ion confinement times at low oxygen content in the interval O = (5–25)% can be understood by analyzing the ion pressure profiles.

In Fig. 8, the dependencies of ion pressure on the z coordinate along the source axis are shown for different oxygen contents of 0 and 5%. The profiles are calculated as

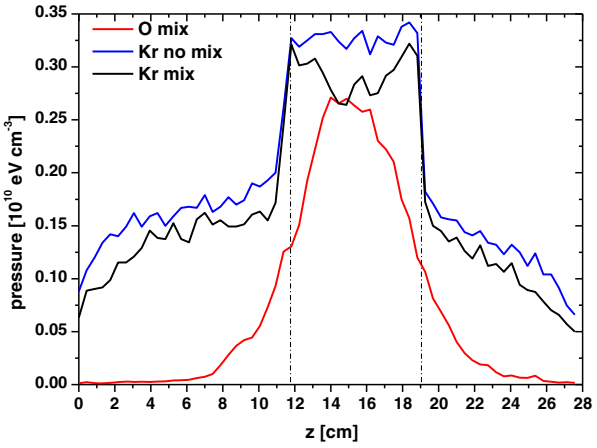

FIG. 8. Ion pressure profiles along the source z axis: pressure of the oxygen ions (red line), pressure of the krypton ions at Kr = 95%, O = 5% (black line), and pressure of the krypton ions at Kr = 100% (blue line).

$P(z) = \sum_i n_{iQ}(z) T_{iQ}(z)$, where the summation is done for all ions of the specific element, krypton or oxygen. The dashed lines indicate the ECR zone positions. For all plasmas, the ion pressure decreases fast outside the ECR zone in directions to both the injection and extraction sides of the source (the injection side is at $z = 0$). For the krypton plasma (O = 0%), the profile is rather flat inside the ECR zone, while for the relatively low oxygen content of 5% the profile of krypton ion pressure is hollow at the source center. At the same time, the oxygen ion pressure is peaked at the center.

The ion density of oxygen is small compared to the density of krypton ions at this small oxygen content, but the oxygen pressure is comparable to the krypton pressure because of high energies of oxygen ions. The oxygen ions push the krypton ions toward the ECR zone boundaries, thus degrading their confinement. When the oxygen content is high, a potential dip starts to be large enough to retard most of the energetic oxygen ions; the oxygen pressure profile inside the ECR volume becomes flat, and its influence on the krypton ion confinement time disappears.

We are not aware of direct experimental measurements of how small amounts of oxygen can influence the source output for the heavy elements. The indirect confirmation of the effect can be that any ECRIS should be conditioned after venting the chamber to reach a good source performance. Apart from changing the source chamber wall conditions, the source conditioning can be connected with the process of removing the residual oxygen and nitrogen molecules out of the source.

We see from Fig. 6 that the potential dip value decreases substantially when a small flux of krypton atoms is injected into the plasma—a krypton content Kr = 5% leads to a decrease of $\Delta\varphi$ from 1.1 to 0.58 V. The result is a loss of confinement for oxygen ions and a decrease in the extracted oxygen currents for the high charge states. In Fig. 9, the charge state distributions for oxygen are shown for an oxygen plasma O = 100% and for the krypton-oxygen mix Kr = 5%, O = 95%. The current of O^{6+} decreases by an order of magnitude.

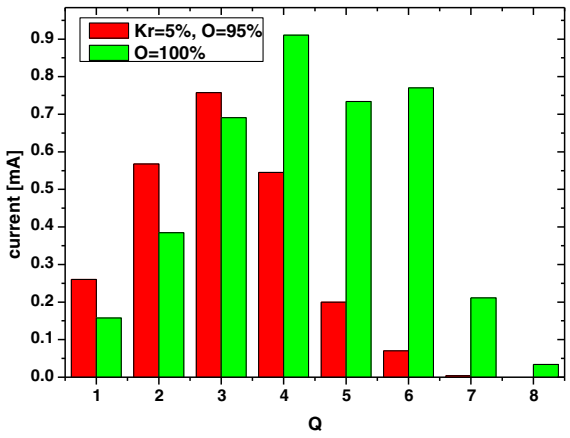

FIG. 9. Charge state distribution of extracted oxygen ion currents for oxygen plasma and for the mix with krypton (Kr = 5%, O = 95%).

Ion temperatures are not the same for different charge states of ions. The general tendency is an increase of the ion temperature with the ion charge state, especially pronounced in the mixed plasmas. The dependences of the temperatures on the charge state are shown in Fig. 10 for the krypton plasma Kr = 100% and for the mix Kr = 15%, O = 85%. For the krypton plasma, the ion temperatures are changing by a factor of 2 comparing the lowly charged (1+) and highly charged (20+) ions. For the mixed plasma, the span in the ion temperatures is much higher, with the temperature of Kr^{1+} ions of around 0.2 eV and of 3 eV for Kr^{20+}. This is an indication of different ion confinement times and different rates of ion energy changes in electron-ion and ion-ion collisions.

The charge state dependences of the ion confinement times are shown in Fig. 11 for the krypton and mixed plasmas.

The confinement time increases with the ion charge state. For the krypton plasma, saturation in the dependence is seen for the high charge states above 10+. In the mix, the confinement times of krypton ions are much higher compared to the nonmixed krypton plasma; the gain is around a factor of ~4. In the same conditions, the confinement times of oxygen ions are much smaller than the times for the krypton ions with the same charge states, reflecting the higher temperatures and the higher mobility of oxygen ions.

The dependencies are fitted with the Rognlien-Cutler-type curves as in Fig. 7. These fits are shown in Fig. 11 as the lines. The fitting coefficient is the same for all curves, $A = 0.74$ m, close to what is calculated for the dependence

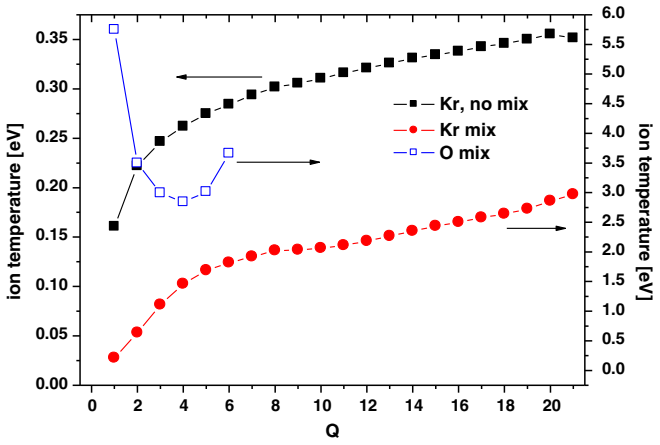

FIG. 10. Charge state dependence of the ion temperature for krypton ions in the pure krypton discharge (left scale, solid black squares) and in the mix of krypton and oxygen (right scale, red circles). Temperatures of oxygen ions are shown as open blue squares (right scale).

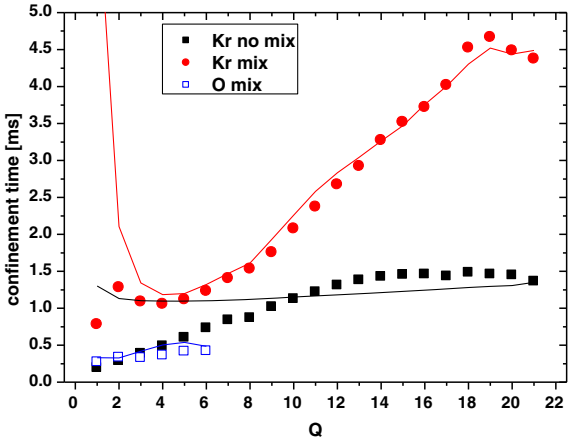

FIG. 11. Confinement times of krypton ions for the krypton plasma (black squares) and in the mix with oxygen (red circles) as a function of the ion charge state. Confinement times of oxygen ions in the mix are shown as the open blue squares. The Rognlien-Cutler fits are shown as the lines.

in Fig. 7. It is seen that the fit greatly overestimates the confinement times for the lowly charged ions in both the mixed ($Q < 2+$) and nonmixed plasmas ($Q < 10+$). A good correspondence between the calculated times and the fit is obtained for the highly charged krypton ions in the mixed plasma.

2. Mixes with other gases

Plasma parameters are also obtained for other mixing gases (N, He, Ne, and Ar) and for the oxygen isotope ^{18}O. The results are listed in Table III, showing the extracted currents of Kr^{18+}, flows of the krypton and mixing gases, currents of the representative ions of the mixing element, potential dip value, the electron confinement time, temperature of Kr^{17+} ions in the ECR volume, temperature of the representative ions of the mixing element, mean electron density in the ECR volume, electron density seen by Kr^{17+} ions, and the confinement time of the Kr^{17+} ions.

There is no statistically significant difference between mixed Kr-O plasmas with an injection of light ^{16}O and heavy ^{18}O isotopes. When using nitrogen as the mix gas, the current of Kr^{18+} is smaller than in the oxygen mix. Also, both the potential dip and the ion temperatures are smaller. The ion confinement time for Kr^{17+} ions with the admixed nitrogen is higher than in the oxygen mix, as well as the ratio between the $\Delta\varphi/T_i(Kr^{17+})$ values (0.155 for the nitrogen and 0.147 for the oxygen mix). Ions are colder in the Kr-N plasma because of two main reasons: a smaller kinetic energy release after the ionization of nitrogen molecules and a larger contribution of the suprathermal nitrogen atoms into the production of the lowly charged nitrogen ions in the dense parts of the ECR plasma. The ions that are produced from the suprathermal nitrogen atoms have relatively low energies and cool the ion population. For nitrogen we use a small recombination coefficient for the production of the molecular nitrogen after atom collisions with the walls. Calculations with the same recombination coefficient as for oxygen (0.5) give the potential dip value of 0.37 V comparable with the value for the oxygen mix. Still, the extracted Kr^{18+} current is smaller in these conditions compared to the oxygen mix.

What makes the oxygen-mixed plasma more efficient for the production and extraction of the highly charged ions of krypton is the spatial distribution of the ion densities, which is hollow but more concentrated toward the source axis compared to the nitrogen case. Indeed, in the oxygen plasma, the mean electron density seen by the krypton highly charged ions is larger by ~10% compared to the nitrogen plasma. The ion distribution at the extraction electrode is more peaked at the source axis—more ions pass through the extraction aperture. The ion densities at the middle of the source along the x axis are plotted in Fig. 12 for oxygen and nitrogen mixes, as well as for the nonmixed krypton plasma, for all krypton ions with $Q \geq 17+$.

The plasma spatial profile is defined by the ambipolar diffusion of particles across the magnetic field due to the electron-ion collisions and by the spatial diffusion of ions caused by the unlike elastic ion-ion collisions [11]. The plasma shape depends, among other factors, on the spatial gradients of the magnetic field, plasma composition, and ion temperatures. Hotter ions in the oxygen-krypton plasma make the profile broader than in the relatively colder nitrogen-krypton mix. For the nonmixed krypton plasma,

TABLE III. Main parameters of the krypton plasmas mixed with different gases. Krypton content is Kr = 15%, $T_{ew} = 12$ keV, $P_{rf} = 500$ W.

Z	Flow (Kr), pmA	Flow (mix), pmA	I_i (Kr^{18+}), μA	$I_i(Q)$, μA	$\Delta\varphi$, V	τ_e, ms	$T_i(17+)$, eV	$T_i(Q)$, eV	n_e, 10^{12} cm^{-3}	$n_e(Kr^{17+})$, 10^{12} cm^{-3}	$\tau_i(Kr^{17+})$, ms
^{16}O	0.06	0.83	40	28(6+)	0.39	0.46	2.64	3.66(6+)	0.73	0.44	4.0
^{18}O	0.06	0.79	38.5	32(6+)	0.39	0.47	2.68	3.52(6+)	0.72	0.45	3.9
N	0.054	0.87	33	63(6+)	0.3	0.48	1.93	2.48(5+)	0.69	0.40	5.1
He	0.074	1.23	12.4	285(2+)	0.022	0.45	0.2	0.21(2+)	0.75	0.79	2.6
Ne	0.051	0.70	19.9	198(6+)	0.05	0.50	0.36	0.38(6+)	0.83	0.57	3.2
Ar	0.047	0.48	13.4	342(8+)	0.06	0.48	0.55	0.54(8+)	0.89	0.62	2.4

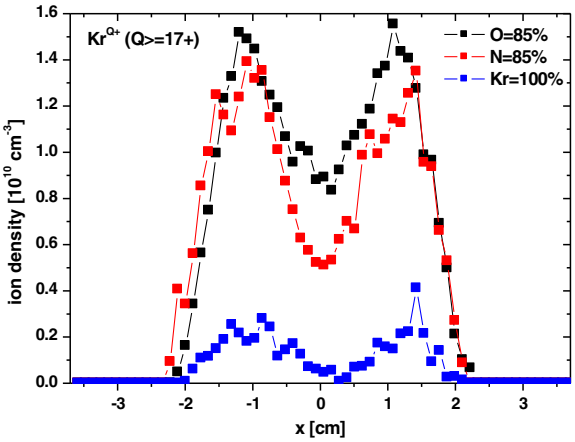

FIG. 12. Density of the krypton ions with the charge states greater and equal to (17+) along the x axis in the middle of the source ($z = 14$ cm) for the mix with oxygen (O = 85%, black) and nitrogen (N = 85%, red) and with no mix (Kr = 100%, blue).

the profile is the sharpest and the ion densities are smallest compared to the mixed plasmas.

We note here that the densities are connected to the extracted ion currents with a scaling factor equal to the ion confinement time ($I_i \sim n_i/\tau_i$) and the ion confinement times are smaller for the nonmixed krypton plasma. The extracted ion currents differ not so much as the ion densities when comparing the mixed and nonmixed plasmas.

Neon is the best among the mixing noble gases, still providing much smaller currents of the krypton highly charged ions and smaller potential dip values than in the oxygen and nitrogen mixes. Argon and helium are less effective as mixing gases compared to neon, with the helium mix resulting in the smallest potential dip values and the smallest current of Kr^{18+} ions.

We conclude by stating that the gas mixing effect in an ECRIS is mainly due to the fact that the plasmas with highly mobile ions need a larger potential barrier to equilibrate the ion and electron loss rates. When the heavy ions are admixed to such plasmas, they are effectively accumulated in the potential trap, which results in their longer confinement times and in a boost in the currents of the highly charged ions.

[1] A. G. Drentje, The ECR ion source and associated equipment at the KVI, Nucl. Instrum. Methods Phys. Res., Sect. B **9**, 526 (1985).

[2] A. G. Drentje, A. Girard, D. Hitz, and G. Melin, Role of low charge state ions in electron cyclotron resonance ion source plasmas, Rev. Sci. Instrum. **71**, 623 (2000).

[3] T. Nakagawa, T. Kageyama, M. Kase, A. Goto, and Y. Yano, Upgrade of RIKEN 10 GHz Electron Cyclotron Resonance Ion Source using plasma cathode method, Jpn. J. Appl. Phys. **32**, L1335 (1993).

[4] Z. Q. Xie and C. M. Lyneis, Plasma potentials and performance of the advanced electron cyclotron resonance ion source, Rev. Sci. Instrum. **65**, 2947 (1994).

[5] T. Lamy, J. Angot, M. Marie-Jeanne, J. Médard, P. Sortais, T. Thuillier, A. Galatà, H. A. Koivisto, and O. A. Tarvainen, Fine frequency tuning of the PHOENIX charge breeder used as a probe for ECRIS plasmas, in *Proceedings of the Nineteenth International Workshop on ECR Sources (ECRIS10)* (LPSC, Grenoble, France, 2010), http://accelconf.web.cern.ch/AccelConf/ECRIS2010/papers/wecobk03.pdf.

[6] A. G. Drentje, Techniques and mechanisms applied in electron cyclotron resonance sources for highly charged ions, Rev. Sci. Instrum. **74**, 2631 (2003).

[7] G. D. Shirkov, A classical model of ion confinement and losses in ECR ion sources, Plasma Sources Sci. Technol. **2**, 250 (1993).

[8] R. Geller, *Electron Cyclotron Resonance Ion Sources and ECR Plasma* (Institute of Physics, Bristol, 1996).

[9] M. Delaunay, Influence of ionization cross sections on the gas mixing effect for the production of Ar^{9+} ions in a CAPRICE ECR source, Rev. Sci. Instrum. **63**, 2861 (1992).

[10] D. Meyer, H. Schmitz, Th. Daube, C. Mannel, and K. Wiesemann, Influence of plasma-wall interaction on high charge state production in electron cyclotron resonance ion sources, Rev. Sci. Instrum. **71**, 660 (2000).

[11] V. Mironov, S. Bogomolov, A. Bondarchenko, A. Efremov, and V. Loginov, Numerical model of electron cyclotron resonance ion source, Phys. Rev. ST Accel. Beams **18**, 123401 (2015).

[12] K. Halbach, Design of permanent multipole magnets with oriented rare earth cobalt material, Nucl. Instrum. Methods **169**, 1 (1980).

[13] A. Efremov, V. Bekhterev, S. Bogomolov, V. Drobin, V. Loginov, A. Lebedev, N. Yazvitsky, and B. Yakovlev, The preliminary tests of the superconducting electron cyclotron resonance ion source DECRIS-SC2, Rev. Sci. Instrum. **83**, 02A334 (2012).

[14] T. D. Rognlien and T. A. Cutler, Transition from Pastukhov to collisional confinement in a magnetic and electrostatic well, Nucl. Fusion **20**, 1003 (1980).

[15] J. D. Huba, NRL Plasma Formulary Report No. NRL/PU/6790-04-477, 2004.

[16] R. F. Post, The magnetic mirror approach to fusion, Nucl. Fusion **27**, 1579 (1987).

[17] V. P. Pastukhov, Collisional losses of electrons from an adiabatic trap in a plasma with a positive potential, Nucl. Fusion **14**, 3 (1974).

[18] B. P. Cluggish, L. Zhao, and J. Kim, Modeling of the stability of electron cyclotron resonance ion source plasmas, Nucl. Instrum. Methods Phys. Res., Sect. A **631**, 111 (2011).

[19] S. Nakazaki, M. Nakashima, H. Takebe, and K. Takayanagi, Energy distribution of secondary electrons in electron-impact ionization of hydrogen-like ions, J. Phys. Soc. Jpn. **60**, 1565 (1991).

[20] F. O. Goodman, Thermal accommodation coefficients, J. Phys. Chem. **84**, 1431 (1980).

[21] J. P. Booth and N. Sadeghi, Oxygen and fluorine atom kinetics in electron cyclotron resonance plasmas by time-resolved actinometry, J. Appl. Phys. **70**, 611 (1991).

[22] G. Oinuma, Y. Inanaga, Y. Tanimura, M. Kuzumoto, Y. Tabata, and K. Watanabe, A comparative study of the surface recombination of nitrogen atoms on various materials at atmospheric pressure, J. Phys. D **43**, 255202 (2010).

[23] G. Cartry, L. Magne, and G. Cernogora, Atomic oxygen recombination on fused silica: Experimental evidence of the surface state influence, J. Phys. D **32**, L53 (1999).

[24] M. Mattioli, G. Mazzitelli, M. Finkenthal, P. Mazzotta, K. B. Fournier, J. Kaastra, and M. E. Puiatti, Updating of ionization data for ionization balance evaluations of atoms and ions for the elements hydrogen to germanium, J. Phys. B **40**, 3569 (2007).

[25] H.-K. Chung, M. H. Chen, W. L. Morgan, Y. Ralchenko, and R. W. Lee, FLYCHK: Generalized population kinetics and spectral model for rapid spectroscopic analysis for all elements, High Energy Density Phys. **1**, 3 (2005).

[26] M. Mattioli, G. Mazzitelli, K. B. Fournier, M. Finkenthal, and L. Carraro, Updating of atomic data needed for ionization balance evaluations of krypton and molybdenum, J. Phys. B **39**, 4457 (2006).

[27] V. P. Shevelko and H. Tawara, Semiempirical formula for multiple ionization cross sections of atoms by electron impact, Phys. Scr. **52**, 649 (1995).

[28] I. N. Bogatu, D. H. Edgell, J. S. Kim, R. C. Pardo, and R. Vondrasek, Argon ionization cross sections for charge state distribution modeling in electron cyclotron resonance ion source, Rev. Sci. Instrum. **73**, 638 (2002).

[29] Y. Itikawa, Cross sections for electron collisions with oxygen molecules, J. Phys. Chem. Ref. Data **38**, 1 (2009).

[30] H. Cherkani-Hassani, D. S. Belic, J. J. Jureta, and P. Defrance, Absolute cross sections for electron impact ionization and dissociation of O_2^+, J. Phys. B **39**, 5105 (2006).

[31] C. H. Sheehan and J.-P. St.-Maurice, Dissociative recombination of N_2^+, O_2^+, and NO^+: Rate coefficients for ground state and vibrationally excited ions, J. Geophys. Res. **109**, A03302 (2004).

[32] Y. Itikawa, Cross sections for electron collisions with nitrogen molecules, J. Phys. Chem. Ref. Data **35**, 31 (2006).

[33] C. Tian and C R Vidal, Electron impact ionization of N_2 and O_2: Contributions from different dissociation channels of multiply ionized molecules, J. Phys. B **31**, 5369 (1998).

[34] J. R. Peterson, A. Le Padellec, H. Danared, G. H. Dunn, M. Larsson, A. Larson, R. Peverall, C. Strömholm, S. Rosén, M. af Ugglas, and W. J. van der Zande, Dissociative recombination and excitation of N_+^2: Cross sections and product branching ratios, J. Chem. Phys. **108**, 1978 (1998).

[35] F. Guzmán, M. O'Mullane, and H. P. Summers, ADAS tools for collisional–radiative modelling of molecules, J. Nucl. Mater. **438**, S585 (2013).

[36] H. Koivisto, O. Tarvainen, V. Toivanen, J. Komppula, R. Kronholm, T. Lamy, J. Angot, P. Delahaye, L. Maunoury, A. Galata, G. Patti, L. Standylo, O. Steczkiewicz, and J. Choinski, Ionization efficiency studies with charge breeder and conventional electron cyclotron resonance ion source, Rev. Sci. Instrum. **85**, 02B917 (2014).

[37] T. Nakagawa, Y. Higurashi, M. Kidera, A. Efremov, V. Mironov, and G. Shirkov, in *Proceedings of the Workshop on the Production of Intense Beams of Highly Charged Ions (PIBHI2000), Catania, Italy, 2000* (Italian Physical Society, Bologna, 2001), p. 105.